J Electr Eng Technol.2018; 13(5): 1935-1944
http://doi.org/10.5370/JEET.2018.13.5.1935

ISSN(Print) 1975-0102
ISSN(Online) 2093-7423

Mathematical Modeling and Control for A Single Winding Bearingless Flywheel Motor in Electric/Suspension Mode

Yuan Ye*, Huang Yonghong†, Xiang Qianwen* and Sun Yukun**

Abstract – With the increase of the production of energy from renewable, it becomes important to look at techniques to store this energy. Therefore, a single winding bearingless flywheel motor (SWBFM) specially for flywheel energy storage system is introduced. For the control system of SWBFM, coupling between the torque and the suspension subsystems exists inevitably. It is necessary to build a reasonable radial force mathematical model to precisely control SWBFM. However, SWBFM has twelve independently controlled windings which leads to high-order matrix transformation and complex differential calculation in the process of mathematical modeling based on virtual displacement method. In this frame, a Maxwell tensor modeling method which is no need the detailed derivation and complex theoretical computation is present. Moreover, it possesses advantages of universality, accuracy, and directness. The fringing magnetic path is improved from straight and circular lines to elliptical line and the rationality of elliptical line is verified by virtual displacement theory according to electromagnetic torque characteristics. A correction function is taken to increase the model accuracy based on finite element analysis. Simulation and experimental results show that the control system of SWBFM with radial force mathematical model based on Maxwell tensor method is feasible and has high precision.

Keywords: Bearingless, Flywheel energy storage, Modeling method, Finite element analysis.

1. Introduction

The flywheel energy storage system (FESS) [1], with its advantages of long life [2], high energy storage density [3], and low rotational loss [4-5], is considered the most competitive and promising energy storage technology especially in the field of renewable energy, and has recently elicited research attention [6-8]. The materials for flywheel, the type of electrical machine [9-10], the type of bearings, and the confinement atmosphere determine the energy efficiency of FESS.

Conventional mechanical bearings are a source of energy losses and require lubrication to relieve mechanical friction, i.e., a fast rotational speed of the flywheel rotor in motoring mode corresponds to a large friction loss because of wearing The flywheel stores mechanical energy that interchanges in the form of electrical energy via an electrical machine/generator with a bidirectional power converter. Thus, the 5 degrees of freedom (DOF) low consumption FESS is realized with 3-DOF magnetic bearings (MB) [10-11] and bearingless motor.

The flywheel in the FESS is rotated by an electric machine that operates as a motor in an electric-energy storage mode. In case of a breakdown of the electric current, the flywheel rotated by its inertia under vacuum conditions makes the electric machine operate as a generator. A reliable, fail-safe, robust, compact and low-cost electric motor is needed for FESS with high temperatures or extreme temperature variations. As the core of the energy conversion unit, the type of motor/generator used for the high-power FESS considerably affects the overall performance of energy storage device. The bearingless switched reluctance motor (BSRM) [12] possesses these characteristics. Given that the stator structure of MB is similar to that of switched reluctance motor (SRM) [13], the bearingless technology is applied to enhance high-speed performance of SRM. BSRM is not only capable of rotating, but also realizes levitation.

Research on BSRM key technologies primarily consists of the following: (1) Mathematical model of radial force and torque [14]. (2) Structure parameter optimization design [15]. (3) Design of control strategy [16]. (4) Optimizing the number of sensors [17]. (5) Suppression for torque ripples and noise [18]. (6) Decoupling control [19]. (7) Fault operation technique [20]. (8) Generation mode research [21-22].

At present, the structure of BSRM is divided into three types-additional suspension winding type, wide/narrow poles type and single winding type. For additional suspension winding type BSRM, the suspension winding increases the complexity of the motor structure and reduces input power utilization. For wide/narrow poles type BSRM, the torque power is sacrificed to realize decoupling control of radial force and torque. For single winding type BSRM,

† Corresponding Author: School of Electrical and Information Engineering, Jiangsu University, China. (hyh@ujs.edu.cn)
* School of Electrical and Information Engineering, Jiangsu University, Zhenjiang, China. (763874393@qq.com)
** School of Power Engineering, Nanjing Institute of Technology, Nanjing, China. (syk@ujs.edu.cn)
Received: December 17, 2017; Accepted: April 6, 2018

the magnitude of the suspension current component is adjusted in real time according to the external disturbance force with the advantages of high efficiency, flexible control and strong fault tolerance.

In this paper, the mathematical modeling and control method for a single winding bearingless flywheel motor (SWBFM) is studied in electric/suspension mode. The coupling between the torque subsystem and the suspension subsystem exists inevitably, thus it is necessary to build a correct radial force mathematical model to realize the precise control of SWBFM. However, SWBFM has twelve independently controlled windings which leads to high-order matrix transformation and complex differential calculation in the process of mathematical modeling based on virtual displacement method. In this frame, a modeling method with Maxwell tensor method is present. The simulation and experimental results show that the mathematical model based on the proposed method is feasible and has high precision.

2. A Novel Bearingless 5-DOF FESS with SWBFM

2.1 A novel bearingless 5-DOF FESS

A novel bearingless 5-DOF FESS with fully integrated structure is shown in Fig. 1. The FESS mainly consists of a bearingless motor, 3-DOF MB and an auxiliary bearing.

Fig. 1(a) shows a novel 5-DOF FESS with characteristics of short axial length, compact structure, flexible control strategy and low loss.

Fig. 1(b) shows the schematic of SWBFM which is made up of and eight poles outer rotor. Twelve poles interior stator is divided into A phase, B phase and C phase. Winding current of each stator pole is controlled independently. i_{a1} is defined as the winding current in A1 pole, i_{a2} is defined as the winding current in A2 pole, i_{a3} is defined as the winding current in A3 pole, i_{a4} is defined as the winding current in A4 pole.

Fig. 1(c) and (d) show the configuration of the 3-DOF MB (axial control coils are hidden in active view) which is made up of a radial stator with four poles, four radial control coils, a rotor lamination, an axial stator with two radial control coils and an axial magnetized permanent magnet.

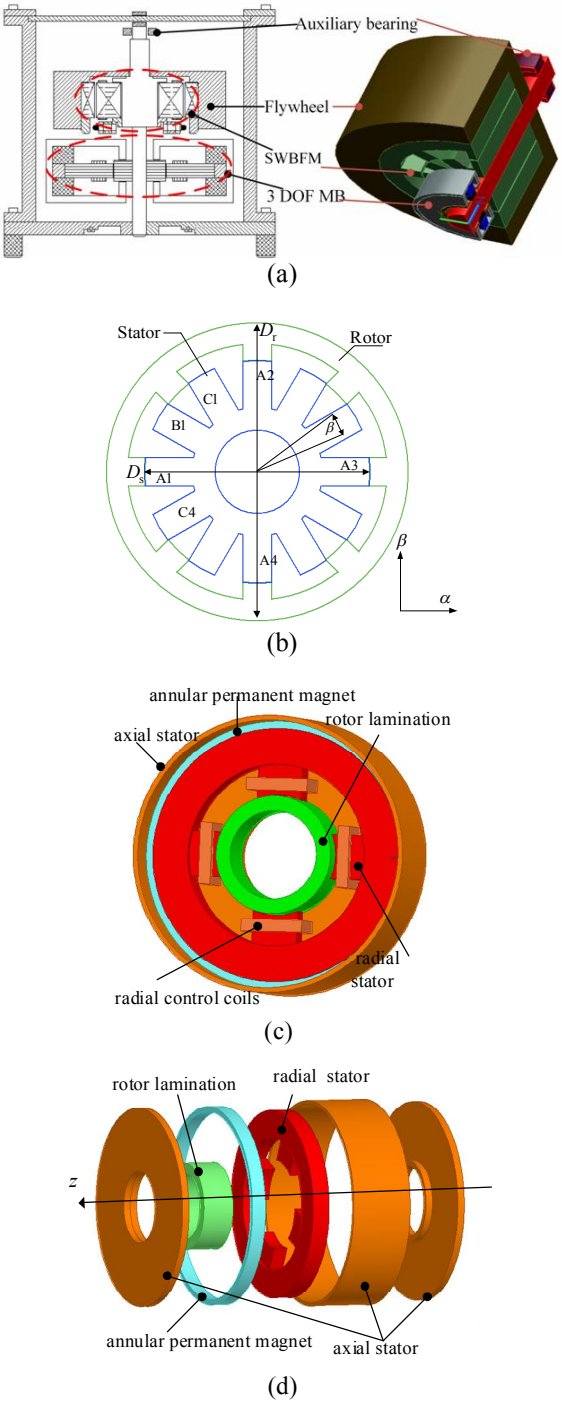

Fig. 1. A bearingless 5-DOF FESS: (a) Overall structure of FESS, (b) Schematic of SWBFM, (c) Configuration of 3-DOF MB, (d) Exploded view of 3-DOF MB

2.2 Principle of radial force generation for SWBFM

The winding current should be equivalent to suspension current component and torque current component. Air gap 1 is defined as the air magnetic circuit between the stator and the rotor of A1 pole. θ is defined as the rotor angular position and θ=0 is the aligned position of the A1 pole. When current i_{a3} is smaller than i_{a1}, the magnetic flux density of air gap 1 is greater than that of air gap and the radial force is generated at the direction of α positive direction. Correspondingly, 2-DOF radial force can be controlled.

Fig. 2 shows the bias magnetic field flux density scalar at θ=-π/12 and θ=0. From Fig. 2(a) and Fig. 2(b), conclusions can be obtained as follows: (1) As the rotor rotates toward to the position, the influence of magnetic saturation is obvious gradually. (2) For phase A, the radial force achieve the maximum value at the aligned position.

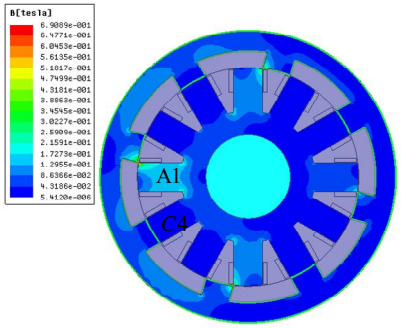

(a)

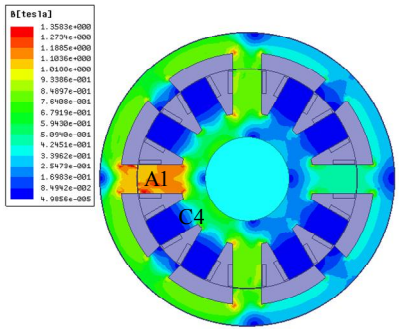

(b)

Fig. 2. Bias magnetic field flux density of SWBFM: (a) Flux density at $\theta=-\pi/12$ (b) Flux density at $\theta=0$

3. Modeling Process for Radial Force

3.1 Modeling method with straight and circular lines

The paths is usually built the with straight-circular lines as shown in Fig. 3 is built.

As in Fig. 3, the integral path surrounds the rotor, and the values of $\Delta d1$, $\Delta d2$ and $\Delta d3$ are approximately equal to zero. The gap permeance P_{a1} can be divided into three parts of permeance P_1, P_2, and P_3, where P_2 and P_3 comprise straight and circular magnetic paths.

The Maxwell force per unit area along a certain dimensional mechanical angle on the rotor surface is expressed as

$$dF(\theta)=\frac{B^2(\theta,t)\cdot dS}{2\mu_0} \tag{1}$$

where μ_0 is the permeability of the vacuum, S is the magnetic field area that surrounds the rotor and B is the magnetic flux density.

The length of the integral path is

$$\begin{cases} l_{12}=l_{34}=l_0, \\ l_{24}+l_{45}=\dfrac{r\pi}{12}-r|\theta|, \\ l_{56}=r|\theta| \end{cases} \tag{2}$$

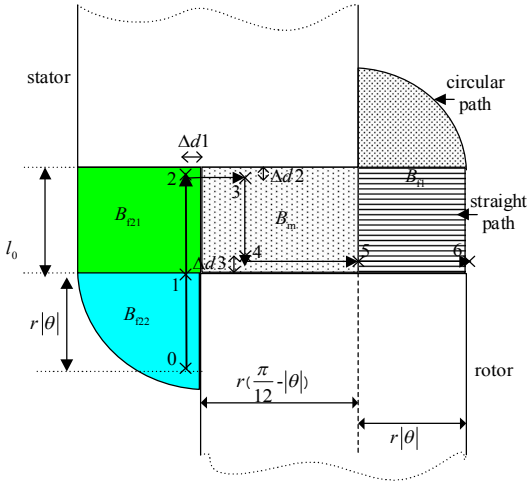

Fig. 3 Paths assumed with straight and circular lines

where l_0 is the air gap length, l_{12}, l_{34}, l_{23}, l_{45}, l_{56} are the selected integral paths and r is the radius of the rotor.

In calculating the radial force, the following assumptions are considered: 1) Magnetic saturation is neglected at the first step of this study. 2) The rotor displacement and air gap length are far less than the rotor radius, i.e., $l_0 << r$ .3) Flux path, which does not link a rotor or flows between stator poles and the rotor interpolar area, can be neglected. 4) Fringing fluxes only at the aligned position are neglected.

Assumptions (1) and (2) allow the radial force expression of one pole to be written as

$$F=\frac{h}{2\mu_0}[(B_{fpt}^2 l_{56}+B_{mpt}^2(l_{23}+l_{45})] \tag{3}$$

where h is the stack length, m is each phase number, and t is each pole number. B_{mpt} is the major magnetic flux density in the overlap area, and B_{fpt} is the fringing magnetic flux. Thus, major magnetic flux density B_{ma1} expressions of the A1 pole is

$$B_{ma1}=\mu_o N i_{a1}/l_0 \tag{4}$$

Fringing magnetic flux density B_{fa1} expressions of the A1 pole is

$$B_{fa1}=\frac{4\mu_0 N i_{a1}}{4l_0+\pi r\theta} \tag{5}$$

Therefore, the radial force F_a produced by the A1 pole is

$$\begin{aligned} F_\alpha &= h[B_{ma1}^2(\pi r/12-r|\theta|)+B_{fa1}^2 r|\theta|]/2\mu_0 \\ &= K_{fa} i_{a1}^2 \end{aligned} \tag{6}$$

where K_{fa} is the radial force coefficient, and

$$K_{fa}=\frac{h}{2\mu_0}[\frac{\mu_0^2N^2(\pi r-12r|\theta|)}{12l_0^2}+\frac{\mu_0^2N^2r|\theta|}{(l_0+\frac{\pi}{4}r|\theta|)^2}] \tag{7}$$

Therefore, the flux ϕ_{a1} of the air gap P_{a1} can be written as

$$\phi_{a1}=P_{a1}U_{a1} \tag{8}$$

where U_{a1} is the magnetic potential difference of the air gap in the A1 pole. Thus, the magnetic energy W_{a1} stored in the A1 pole can be derived as

$$W_{a1}=\frac{1}{2}\phi_{a1}U_{a1}=\frac{1}{2}P_{a1}U_{a1}^2 \tag{9}$$

On the basis of the virtual displacement method, the torque T_{a1} produced at the A1 pole can be derived from the derivative of the magnetic energy W_{a1} with respect to the rotor angular position θ. T_{a1} can be derived as follows:

$$T_{a1}=\frac{\partial W_{a1}}{\partial\theta}=\frac{1}{2}\frac{\partial P_{a1}}{\partial\theta}U_{a1}^2 \tag{10}$$

where T_{a1} is a function of the rotor angular position θ and is proportional to $\frac{\partial P_{a1}}{\partial\theta}$.

The derivative of P_{a1} can be expressed as

$$g(\theta)=\frac{\partial P_{a1}}{\partial\theta}=\frac{\partial P_1}{\partial\theta}+\frac{\partial P_2}{\partial\theta}+\frac{\partial P_3}{\partial\theta} \tag{11}$$

where,

$$\begin{cases} P_1=\int_0^{\frac{\pi}{12}-\theta}\frac{\mu_0hr}{l_0}d\theta, \\ \frac{\partial P_1}{\partial\theta}=-\frac{\mu_0hr}{l_0} \end{cases} \tag{12}$$

$$\begin{cases} P_2=P_3=\int_0^{\theta}\frac{\mu_0hr}{l_0+\frac{\pi}{4}r\theta}d\theta, \\ \frac{\partial P_2}{\partial\theta}=\frac{\partial P_3}{\partial\theta}=\frac{\mu_0hr}{l_0+\frac{\pi}{4}r\theta} \end{cases} \tag{13}$$

The instantaneous torque at the aligned position should be zero based on the torque basic characteristics, i.e., when θ=0, $g(0)=\frac{\partial P_{a1}}{\partial\theta}$=0. However, when $\theta\to0^-$ and $\theta\to0^+$, one obtains

$$\begin{cases} g(0^-)=\frac{\partial P_{a1}}{\partial\theta}=\frac{\partial P_1}{\partial\theta}+\frac{\partial P_2}{\partial\theta}+\frac{\partial P_3}{\partial\theta}=-\frac{\mu_0hr}{l_0} \\ g(0+)=\frac{\partial P_{a1}}{\partial\theta}=\frac{\partial P_1}{\partial\theta}+\frac{\partial P_2}{\partial\theta}+\frac{\partial P_3}{\partial\theta}=\frac{\mu_0hr}{l_0} \end{cases} \tag{14}$$

That is,

$$g(0)\neq g(0^-)\neq g(0+) \tag{15}$$

With (15) and (10) combined, the calculation value of the torque derived using the straight lines and the circular lines is not zero and continuous at the aligned position. This problem must be solved by revising the flux path to realize a stable control system.

3.2 Fringing magnetic path assumed with elliptical line

The improved flux path with elliptical line is shown in Fig. 4. In Fig. 4(a), the which the semi-minor axis of the elliptical line is defined as $r\theta$, and the semi-major axis is expressed as $l_0+kr\theta$

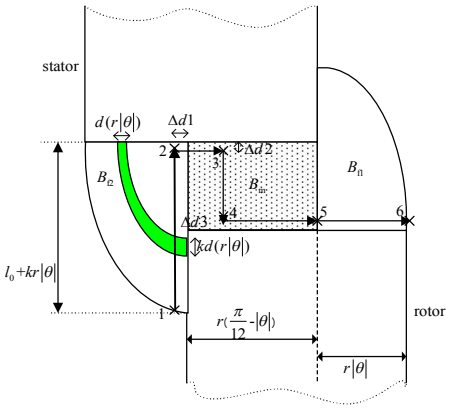

(a)

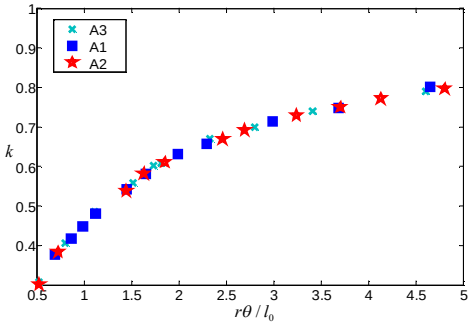

(b)

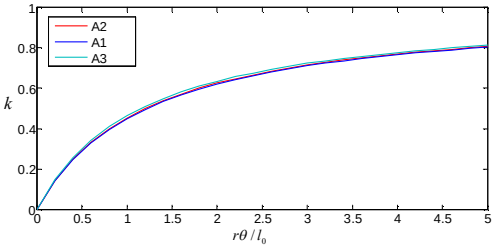

(c)

Fig. 4. Fringing magnetic path assumed with elliptical line: (a) Improved path; (b) Numerical distribution with FEA; (c) LS fitting with numerical distribution

Accordingly, the average cross section area S of dP_3 or dP_2 can be approximated as

$$S = \frac{h(k+1)r}{2} d\theta \tag{16}$$

FEA and least squares (LS) fitting are combined to obtain the relationship of k and $r\theta / l_0$ when $\theta = \pi / 24$ in Fig. 4(b) and Fig.4(c).

The conditions of FEA are shown in Table 1.

Table 1. FEA conditions

	i_{a1}	i_{a2}	i_{a13}	i_{a41}	θ	FEA
conditionA1	7A	3A	3A	7A	$-\pi/24$	1ms
conditionA2	7A	3A	7A	3A	$-\pi/24$	1ms
conditionA3	7A	0A	0A	0A	$-\pi/24$	1ms

On the basis of Fig.4 (b), k is a function of $r\theta / l_0$, approximately: $k = r\theta / l_0 a + r\theta$. Fig. 4(c) indicates that the value of a is 1.2 in condition A1, the value of a is 1.22 in condition A2, and the value of a is1.19 in condition A3. Thus, a can be considered a constant calculated with LS. In this paper, a can be derived as 1.2. Consequently,

$$\frac{\partial P_2}{\partial \theta} = \frac{\partial P_3}{\partial \theta} = \frac{\mu_0 h(al_0 + 2r\theta)}{(al_0 + r\theta)(2l_0 + \frac{\pi}{2}\mathrm{r}\theta)} \tag{17}$$

With Formulas (10), (11), (12), and (17) combined, if the fringing magnetic path is assumed with an elliptical line, when θ=0, then $g(0) = g(0^-) = g(0+)$ and $T_{a1} = 0$ are obtained.

On the basis of the Maxwell tensor method, the length of fringing magnetic path l_1^* is as follows:

$$l_1^* = l_0 + \frac{\pi}{4} kr\theta \tag{18}$$

The improved torque T_{a1} in the A1 pole expression is:

$$T_{a1}(i_{a1}, \theta) = \frac{\mu_0 N^2 hr}{2} \left(\frac{l_0 + kr\theta}{(l_0 + \frac{\pi}{4} kr\theta)^2} - \frac{1}{l_0} \right) i_{a1}^{\ 2} \tag{19}$$

The improved torque T_{a1} possesses the property: $T(i_{a1}, 0) = T(i_{a1}, 0^-) = T(i_{a1}, 0^+) = 0$, which verifies the rationality of the fringing magnetic path using an elliptical line.

3.3 Modeling for radial force

The integral path in Fig. 6 indicates that the radial force mathematical model for the A1 pole can be derived as

$$F_{a1}^{\ *} = \frac{h}{2\mu_0} [(B_{fa1}^2 l_{56} + B_{ma1}^2 (l_{23} + l_{45})] = K_{a1} i_{a1}^{\ 2} \tag{20}$$

Consequently, the radial force mathematical model in α direction is derived as

$$\begin{aligned} F_\alpha^* &= \frac{h}{2\mu_0} [(B_{fa1}^2 l_{56} + B_{ma1}^2 (l_{23} + l_{45})] \\ &= K_a (i_{a1}^{\ 2} - i_{a3}^{\ 2}) \end{aligned} \tag{21}$$

where i_{a3} is the current of A3 pole in A phase, and

$$K_a = K_{a1} = \frac{h}{2\mu_0} \left[\frac{\mu_0^2 N^2 (\pi r - 12r|\theta|)}{12 l_0^2} + \frac{\mu_0^2 N^2 r|\theta|}{(l_0 + \frac{\pi}{4} kr|\theta|)^2} \right] \tag{22}$$

$$k = \frac{r\theta}{1.2 l_0 + r\theta} \tag{23}$$

In order to verify the accuracy of radial force mathematical model, conditions 1, 2, 3, and 4 are taken into consideration in Table 2 based on FEA.

Table 2. Conditions 1, 2, 3, and 4

	i_{a1}	i_{a2}	i_{a3}	i_{a4}	FEA
condition1	2A	1A	0A	1A	1ms
condition2	4A	2A	0A	2A	1ms
condition3	6A	3A	0A	3A	1ms
condition4	8A	4A	0A	4A	1ms

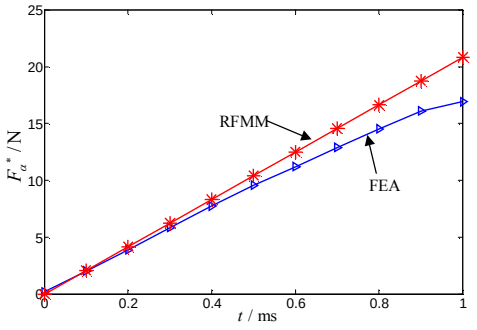

(a)

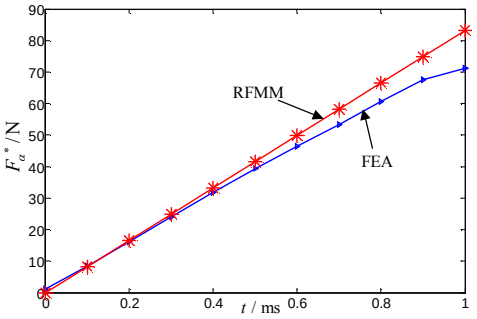

(b)

Fig. 5. Contrast of RFMM and FEA: (a) Contrast of RFMM and FEA in condition 1; (b) Contrast of RFMM and FEA in condition 2

The numerical value contrasts of radial force mathematical model (RFMM) and FEA in conditions 1 and condition 2 are shown in Fig.5.

When $\theta = 0$, the maximum values of calculated RFMM and FEA results are 20 N and 16.5 N in condition 1, and the maximum values of the calculated RFMM and FEA results are 82 N and 70 N in condition 2, which indicates that the FEA results do not agree well with the calculated radial force mathematical model and the relative error is roughly 12%. Nevertheless, when θ=-π/12, the minimum values of the calculated results and the FEA results are equivalent and approach zero.

Above analysis shows that the RFMM is not accurate due to the following factors: 1) The radial force produced by core (except stator pole) and the rotor pole is neglected. 2) The accuracy of the Maxwell tensor method depends on the selection of the integral path, and the line that connects the element that surrounds the rotor pole would also cause certain errors

Thus, a correction factor $k^*(\theta)$ is necessary to revise the radial force expression,

$$F_\alpha = k^*(\theta)K_a[i_{a1}^2 - i_{a3}^2] \tag{24}$$

The correction function $k^*(\theta)$ is derived by LS fitting as

$$k^*(\theta)=-0.7038\theta^2 - 0.819\theta + 0.8136 \tag{25}$$

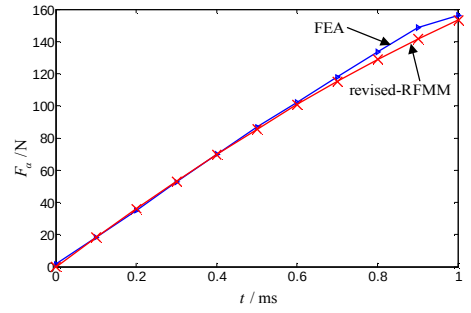

(a)

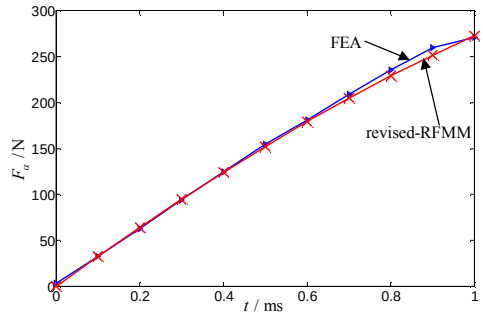

(b)

Fig. 6. Contrast of revised-RFMM and FEA: (a) Contrast of revised-RFMM and FEA in condition 3; (b) Contrast of revised-RFMM and FEA in condition 4

Fig. 6 shows the contrast of the revised radial force mathematical model (revised-RFMM) and FEA in conditions 3 and condition 4.

When $\theta = 0$, the maximum values of calculated revised-RFMM and FEA results are 156.33 N and 157 N in condition 3, and the maximum values of the calculated revised-RFMM and FEA results are 270.7 N and 269 N in condition 4, which indicates that the FEA results agree well with the calculated radial force mathematical model, and the relative error is roughly 2.5%.

Moreover, the minimum values of the calculated results and the FE results are still equivalent and approach zero. The correctness of the model and the feasibility of the method are verified. The expression of radial force based on the Maxwell tensor method has been revised.

The bold dotted line indicates that rotor eccentricity occurred only in the α direction and that the eccentricity length is α. The bold solid line means that rotor eccentricity occurred in both in the α and β directions and that eccentricity lengths are α and β, respectively.

With the rotor eccentricity only in the α direction, l_g can be expressed as follows:

$$l_g = l_0 - \alpha \tag{26}$$

For rotor eccentricity both in the α and β directions, on the basis of the geometrical relationship in Fig. 10, usually, $\theta << \frac{\pi}{2}$ and $\alpha, \beta << r$, which obtains

$$\cos(\angle O_2O_1B) = \frac{|\theta|}{2} + \frac{\beta}{2r} \tag{27}$$

Consequently, with the use of the cosine theorem, in triangle O_2O_1B, the following is obtained:

$$l_g + r = \sqrt{\beta^2 + (l_0 - \alpha + r)^2 - 2\beta(l_0 - \alpha + r)(\frac{|\theta|}{2} + \frac{\beta}{2r})} \tag{28}$$

Thus, with rotor eccentricity both in the α and β directions, l_g can be expressed as follows:

$$l_g = l_0 - \alpha - \frac{|\theta|}{2}\beta \tag{29}$$

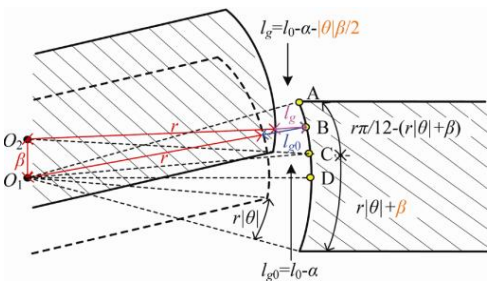

Fig. 7 Calculation relation schema of average length

In general, the radial force mathematical model based on the proposed method is

$$\begin{cases} F_\alpha = k^*(\theta)K_a[i_{a1}^2 - i_{a3}^2] \\ K_a = K_{a1} = \dfrac{h}{2\mu_0}[\dfrac{\mu_0^2 N^2(\pi r - 12r|\theta|)}{12l_g^2} + \dfrac{\mu_0^2 N^2 r|\theta|}{(l_g + \dfrac{\pi}{4}kr|\theta|)^2}] \\ k^*(\theta) = -0.7038\theta^2 - 0.819\theta + 0.8136 \\ l_g = l_0 - \alpha - \dfrac{|\theta|}{2}\beta \end{cases} \quad (30)$$

4. Simulation and Experiment

Since SWBFM is applied in 5-DOF FESS, it has three operation modes: electric/suspension mode in energy storage stage, no load mode in standby stage and generation / suspension mode in energy release stage. In the paper, control strategy is reached for electric/suspension mode with 15° working interval of each phase winding.

Fig. 8 shows the control system diagram of SWBFM which consists of a torque subsystem and a suspension subsystem. A position/speed sensor is used to obtain the rotor position signal and four displacement sensors are applied to track the radial displacement of the rotor in two degree of freedom (β direction and α direction). Coupling between the torque subsystem and the suspension subsystem exists inevitably, i.e., radial force model and torque model need to be considered in the modeling process. SWBFM has twelve independently controlled windings which leads to high-order matrix transformation and complex differential calculation in the process of mathematical modeling based on virtual displacement method. Maxwell stress method with the advantages of universality, accuracy, and directness does not need detailed derivation and complex theoretical computation.

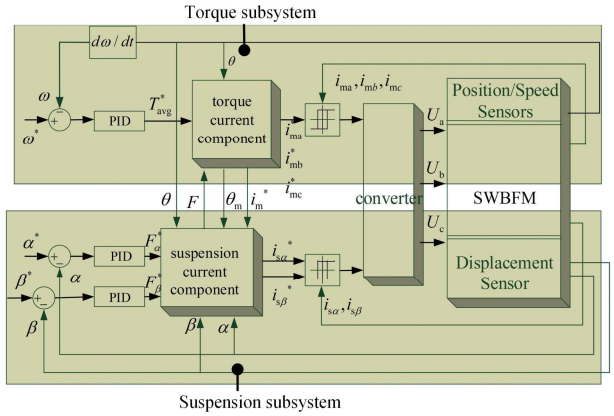

(a)

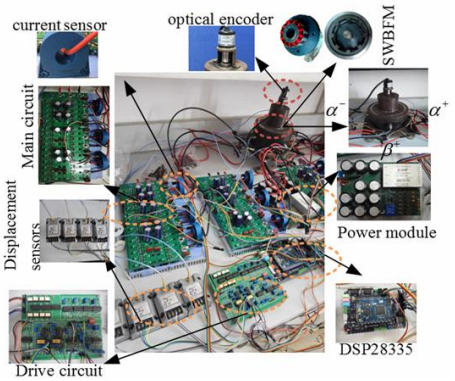

(b)

Fig. 8. Control system diagram of SWBFM: (a) Control principle diagram; (b) Experiment platform

The A phase current control strategy can be expressed as

$$\begin{cases} i_{A1} = i_{ma} + i_{sa\alpha} \quad i_{A3} = i_{ma} - i_{sa\alpha} \\ i_{A2} = i_{ma} + i_{sa\beta} \quad i_{A4} = i_{ma} - i_{sa\beta} \end{cases} \quad (31)$$

where $i_{sa\alpha}$, $i_{sa\beta}$ are the suspension current components and i_{ma} is the torque current component

Consequently, it yields

$$\begin{cases} F_\alpha = 4k^*(\theta)K_a i_{ma} i_{sa\alpha} \\ F_\beta = 4k^*(\theta)K_a i_{ma} i_{sa\beta} \end{cases} \quad (32)$$

and the synthetic radial force can be expressed as

$$F^2 = F_\alpha^{\,2} + F_\beta^{\,2} = 16K_f^{\,2} i_{ma}^{\,2} i_{sa}^{\,2} \quad (33)$$

where $i_{sa}^{\,2} = i_{sa\alpha}^{\,2} + i_{sa\beta}^{\,2}$, $K_f^{\,2} = k^*(\theta)^2 K_a^{\,2}$.

Similarly, torque mathematical model of A phase is

$$T_a = \begin{cases} \dfrac{\mu_0 N^2 hr}{2}(-\dfrac{l_0 + kr\theta}{(l_0 + \dfrac{\pi}{4}kr\theta)^2} + \dfrac{1}{l_0})\left(i_{a1}^{\,2} + i_{a2}^{\,2} + i_{a3}^{\,2} + i_{a4}^{\,2}\right), T_a \geq 0 \\ \dfrac{\mu_0 N^2 hr}{2}(\dfrac{l_0 + kr\theta}{(l_0 + \dfrac{\pi}{4}kr\theta)^2} - \dfrac{1}{l_0})\left(i_{a1}^{\,2} + i_{a2}^{\,2} + i_{a3}^{\,2} + i_{a4}^{\,2}\right), T_a < 0 \end{cases} \quad (34)$$

The advanced angle θ_m is the angle from the middle point of the conduction period of square-wave current to the aligned position of rotor and stator poles, θ_{on} is the turn-on angle and θ_{off} is the turn-off angle. It yields

$$\begin{cases} \theta_{on} = -\dfrac{\pi}{24} - \theta_m, \quad \theta_{off} = \dfrac{\pi}{24} - \theta_m \end{cases} \quad (35)$$

Combine (35), (37) and (38), it yields

$$T_{avg} = G_t(\theta_m) i_{ma}^2 + G_s(\theta_m)\frac{F^2}{i_{ma}^2} \quad (36)$$

where $G_t(\theta_m) = 2CA$, $G_s(\theta_m) = \dfrac{1}{16K_{f0}^2}CA$,

$$a_1 = l_0 - \frac{\pi}{4}kr(-\frac{\pi}{24}-\theta_{\mathrm{m}}),\ a_2 = l_0 + \frac{\pi}{4}kr(\frac{\pi}{24}-\theta_{\mathrm{m}}),$$

$$K_{f0}^2 = K_{f|\theta=0}^2,\quad C=\frac{6\mu_0 N^2 hr}{\pi}.$$

$$A=\left[\frac{4l_0}{\pi kr}(\frac{1}{a_1}-\frac{1}{a_2})-\frac{4}{\pi}\left(\frac{\left(-\frac{\pi}{24}-\theta_m\right)}{a_1}+\frac{\left(\frac{\pi}{24}-\theta_m\right)}{a_2}\right)\right.$$
$$\left.+\frac{16}{\pi^2 kr}\ln\left(\frac{a_2}{a_1}+2\frac{\theta_m}{l_0}\right)\right]$$

The maximum radial force formula is:

$$F_{\mathrm{m}}^2 = 16K_f{}^2(\theta_{\mathrm{on}})i_{\mathrm{mm}}^2 i_{\mathrm{sam}}^2 \tag{37}$$

The maximum average torque formula is:

$$T_{\mathrm{avg}\,m} = \frac{12}{\pi}\int_{\theta_{\mathrm{on}}}^{\theta_{\mathrm{off}}} J_t N^2(2i_{\mathrm{m}\,m}^2 + \Delta i_{sam}{}^2)d\theta \tag{38}$$

where i_{mm} is the amplitude of i_{ma}, i_{sam} is the amplitude of $i_{sa\alpha}$ and $i_{sa\beta}$

Rewriting formula (39), it yields

$$i_{\mathrm{ma}} = \sqrt{\left(T_{\mathrm{avg}} + \sqrt{T_{\mathrm{avg}}^2 - P}\right)/2G_t(\theta_{\mathrm{m}})} \tag{39}$$

Where $P=T_{\mathrm{avg}}^2 - 4G_t(\theta_m)G_s(\theta_m)F^2$.

4.1 Simulation

Fig. 9 shows the simulation waveforms of currents and displacements for SWBFM.

Fig. 9(a) shows the displacement in α direction and β direction. Fig. 9(b) shows the twelve winding currents in A phase, B phase and C phase. It is seen that under the related control system and control strategy, the displacement fluctuation in α direction and β direction is much smaller than the value of the air gap. The electric/levitation function for SWBFM is realized.

4.2 Experiment

Fig. 10 shows the displacement waveforms of the rotor based on the mathematical model proposed in this paper.

Motor speed is accelerated from 2000 r/min to 5000 r/min. As shown in Fig. 10(a) and 10(b), the fluctuation of unilateral eccentricity in the α and β directions is approximately 40 μm at the speed of 2000 r/min, 16% of the length of the air gap. As shown in Figs. 10(b) and 10 (c), the fluctuation of unilateral eccentricity in the α and β directions is approximately 50 μm at the speed of 5000

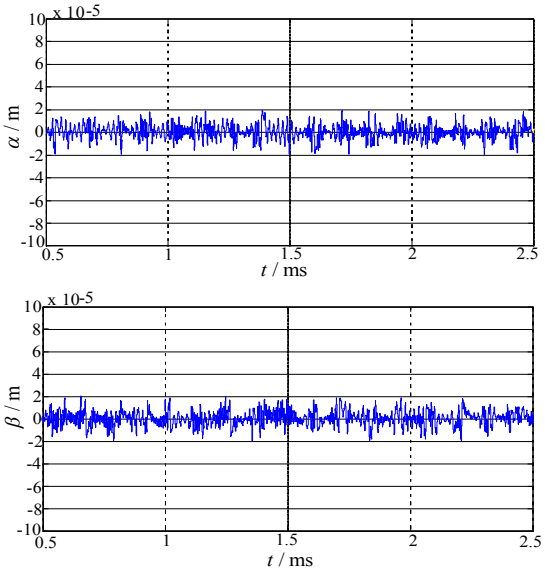

(a)

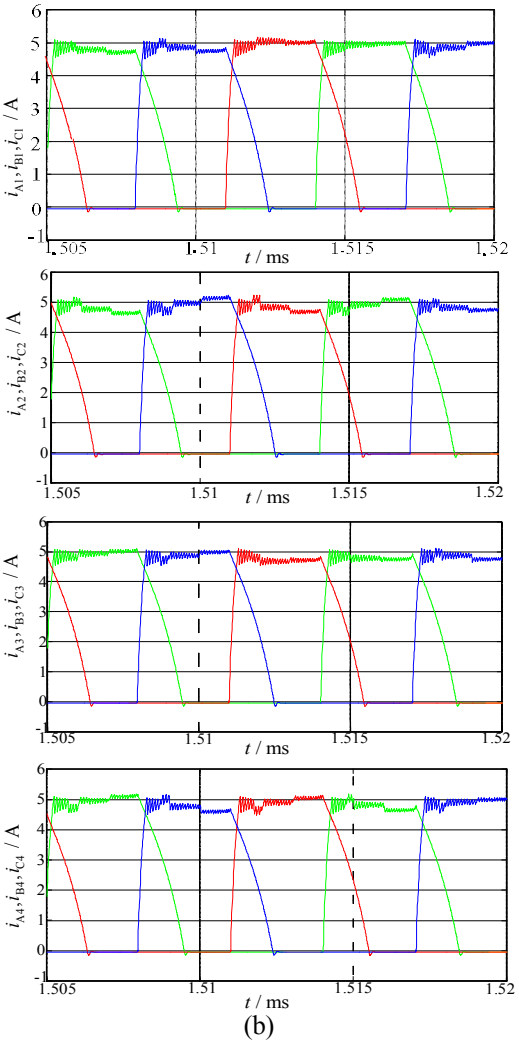

(b)

Fig. 9. Simulation waveforms of currents and displacements: (a) Displacement waveforms in electric/suspension mode; (b) Current waveforms of 12 poles windings

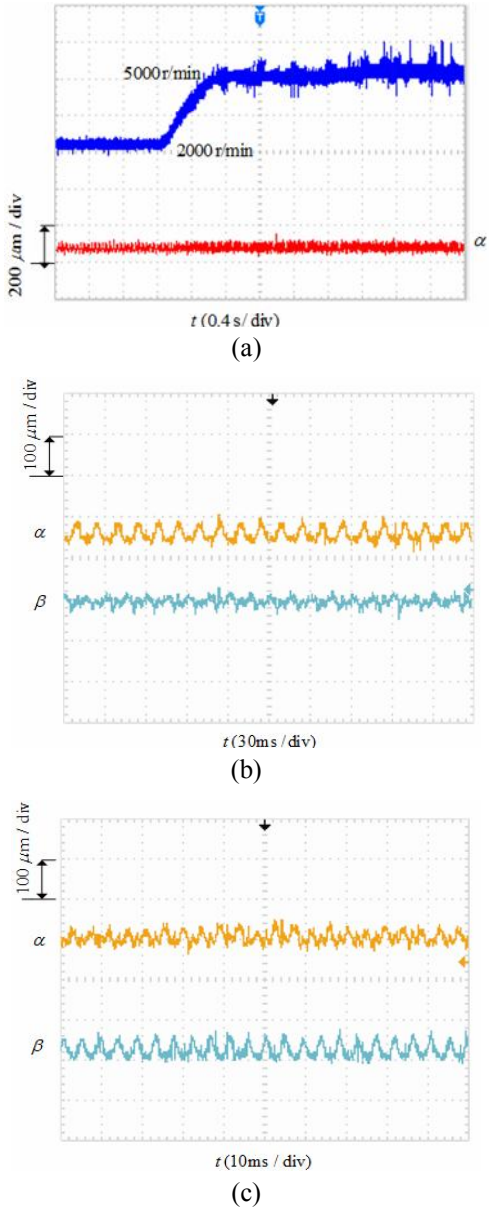

Fig. 10. Experimental waveforms in α and β direction: (a) Acceleration waveforms from 2000 r/min to 5000 r/min; (b) Experimental waveforms at a speed of 2000 r/min; (c) Experimental waveforms at a speed of 5000 r/min

r/min, 20% of the length of the air gap. The eccentricity fluctuation is far less than the length of the air gap. Experimental results show that the radial force mathematical model based on the Maxwell tensor method with improved fringing magnetic path is feasible and has high precision.

5. Conclusion

It differs from the conventional virtual displacement methods (equivalent magnetic circuit), the proposed method based on the Maxwell tensor method in this paper has the advantages of universality, accuracy, and directness. During the modeling process, we do not need to derive the equivalent magnetic circuit model after intensive analysis

(1) Before the radial mathematical model is established, the fringing magnetic path is improved from straight and circular lines to elliptical lines, and the rationality is verified. (2) The influence of rotor eccentricity in two DOF is considered, and a correction function is taken to obtain an accurate radial mathematical model based on FEA. The expression of radial force mathematical model has been verified by the FEA experimental results. (3) The proposed modeling method also provides a guide for other structures and types of bearingless switched reluctance motor.

Acknowledgements

This work was supported by the National Natural Science Foundation of China (51707082, 51607080), Natural Science Foundation of Jiangsu Province (BK20170546, BK20150510), China Postdoctoral Science Foundation (2017M620192) and the Priority Academic Program Development of Jiangsu Higher Education Institutions.

References

[1] O'Sullivan Dara L., and A. W. Lewis., "Generator Selection and Comparative Performance in Offshore Oscillating Water Column Ocean Wave Energy Converters," *IEEE Transactions on Energy Conversion*, vol. 26, no. 2, pp. 603-614, 2011.

[2] Sarkar S., and V. Ajjarapu, "MW resource assessment model for a hybrid energy conversion system with wind and solar resources," *IEEE Transactions on Sustainable Energy*, vol. 2, no. 4, pp. 383-391, 2011.

[3] Casella F., "Modeling, simulation, control, and optimization of a geothermal power plant," *IEEE Transactions on Energy Conversion*, vol. 19, no. 1, pp. 170-178, 2004.

[4] Yuan Y., Y. Sun and Huang Y., "Accurate mathematical model of bearingless flywheel motor based on Maxwell tensor method," *ELECTRONICS LETTERS*, vol. 52, no. 11, pp. 950-952, 2016.

[5] Zhan C. and Tseng K., "A novel flywheel energy storage system with partially-self-bearing flywheel-rotor," *IEEE Transactions on Energy Conversion*, vol. 22, no. 2, pp. 477-487, 2007.

[6] Subkhan M. and Komori M., "New Concept for Flywheel Energy Storage System Using SMB and PMB," *IEEE Transactions on Applied Superconductivity*, vol. 21, no. 3, pp. 1485-1488, 2011.

[7] Wei K., Liu D. and Meng J, "Design and Simulation of a 12-Phase flywheel energy storage generator system with linearly dynamic load," *IEEE Transactions*

on Applied Superconductivity, vol. 20, no. 3, pp. 1050-1055, 2010.
[8] Cimuca G., Breban S. and Mircea M, "Design and control strategies of an induction-machine-based flywheel energy storage system associated to a variable-speed wind generator," *IEEE Transactions on Energy Conversion*, vol. 25, no. 2, pp. 526-534, 2010
[9] Abdi B., Hamid B. and Mirtalaei M., "Simplified design and optimization of slotless brushless DC machine for micro-satellites electro-mechanical batteries," *Journal of Electrical Engineering and Technology*, vol. 8, no. 1, pp. 124-129, 2013.
[10] Kim J., Choi J. and Lee S, "Experimental Evaluation on Power Loss of Coreless Double-side Permanent Magnet Synchronous Motor/Generator Applied to Flywheel Energy Storage System," *Journal of Electrical Engineering & Technology*, vol. 12, no. 1, pp. 256-261, 2017.
[11] Morrison C., Siebert M. and Ho E., "Electromagnetic Forces in a Hybrid Magnetic-Bearing Switched-Reluctance Motor," *IEEE Transactions on Magnetics*, vol. 44, no. 22, pp. 4626-4638, 2008.
[12] Yuan Y., Sun Y. and Huang Y., "Variable saturation soft variable structure control of magnetic bearing," *Control Theory & Applications*, vol. 32, no. 12, pp. 1627-1634, 2010.
[13] Takemoto M., Chiba A. and Akagi H., "Radial force and torque of a bearingless switched reluctance motor operating in a region of magnetic saturation," *IEEE Transaction. Industry Applications*, vol. 40, no. 1, pp. 103-112, 2004.
[14] Rallabandi V. and Fernandes B., "Design procedure of segmented rotor switched reluctance motor for direct drive applications," *IET Electric Power Applied*, vol. 8, no. 3, pp. 77-88, 2014.
[15] Cao X., Deng Z., Yang G., "Mathematical model of bearingless switched reluctance motors based on Maxwell stress tensor method," *Proceedings of the CSEE*, vol. 29, no. 3, pp. 78-83, 2009.
[16] Yang G., Deng Z., Cao X., "Optimal winding arrangements of a bearingless switched reluctance motor," *IEEE Transactions on Power Electronics*, vol. 23, no. 6, pp. 3056-3066, 2008.
[17] Yang Y., Deng Z., Cao X., "A control strategy for bearingless switched-reluctance motors," *IEEE Transactions on Power Electronics*, vol. 25, no. 11, pp. 2807-2819, 2010.
[18] Zhu Z., Sun Y., "Displacement and position observers designing for bearingless switched reluctance motor," *Proceedings of the CSEE*, vol. 32, no. 12, pp. 83-89, 2012.
[19] Yang Y., Deng Z., "Effects of control strategies on stator vibration of bearingless switched reluctance motors," *Acta Aeronautica Et Astronaut Ica Sinica*, vol. 31, no. 10, pp. 2010-2017, 2010.
[20] Liu X., Sun Y., Wang D., "Decoupling and variable structure control for radial displacement of bearingless switched reluctance motors," *Transactions of the Chinese Society for Agricultural Machinery*, vol. 38, no. 9, pp. 147-150, 2007.
[21] Yuan Y., Sun Y., Huang Y., "Radial force dynamic current compensation method of single winding bearingless flywheel motor," *IET Power Electronics*, vol. 8, no. 7, pp. 1224-1229, 2015.
[22] Cao X., Deng Z., Zhuang Z., "Principle and implementation of a bearingless switched reluctance generator with three adjacent excitation-windings connected in series," *Transactions of China Electro-technical*, vol. 28, no. 2, pp. 108-116, 2013.
[23] Cao X., Deng Z., "A full-period generating mode for bearingless switched reluctance generators," *IEEE Transactions on Applied Superconductivity*, vol. 20, no. 3, pp. 1072-1076, 2010.

Ye Yuan He was born in 1991 and received PhD degree in electrical engineering from Jiangsu University. His research interests include bearing-less motor design and control.

Yong-Hong Huang She was born in 1970 and received PhD degree in electrical engineering from Jiangsu University. Her research interest is motor control for new energy vehicle.

Qian-Wen Xiang She was born in 1980 and received PhD degree in electrical engineering from Jiangsu University. Her research interests include motor intelligent design and optimization.

Yu-kun Sun He was born in 1958 and received PhD degree in electrical engineering from Jiangsu university. His research interest is special motor design.